

A Coupled Thermo-Mechanical Model for Simulating the Material Failure Evolution Due to Localized Heating

Z. Chen^{1,2}, Y. Gan¹ and J.K. Chen²

Abstract: A coupled thermo-mechanical constitutive model with decohesion is proposed to simulate the material failure evolution due to localized heating. A discontinuous bifurcation analysis is performed based on a thermoviscoplasticity relation to identify the transition from continuous to discontinuous failure modes as well as the orientation of the discontinuous failure. The thermo-mechanical model is then implemented within the framework of the Material Point Method (MPM) so that the different gradient and divergence operators in the governing differential equations could be discretized in a single computational domain and that continuous remeshing is not required with the evolution of failure. The proposed model-based simulation procedure is verified with analytical solutions available, and the potential of the proposed procedure is demonstrated by simulating the material failure evolution in a prestressed plate subject to laser irradiation.

Keyword: Failure evolution, localized heating, decohesion, bifurcation, MPM.

1 Introduction

Severe localized thermal loads due to quenching, aerodynamic heating, laser irradiation etc. may lead to local material failure and even global structural failure. To improve the relevant design methodology, hence, a fundamental understanding is required on the material failure evolution due to localized high-energy loading. As

can be found from the open literature, many efforts have been made to investigate the thermo-mechanical failure based on the traditional thermoelasticity/thermoplasticity theories and linear elastic fracture mechanics (LEFM). For example, the fracture pattern due to a localized moving heat source has been investigated by the maximum circumferential stress criterion [Erdogan and Sih (1963)] and the minimum strain energy density criterion [Sih (1973)]. Beraun, Chen and Tzou (1999) studied the thermo-mechanical fracture of a pressurized vessel subject to the impingement of a point heat source, with the use of the stress and strain-energy-based criteria. In LEFM, the crack behavior such as crack direction is assumed to be only dependent on the magnitudes of the stress intensity factors. Various methods have been used to calculate the stress intensity factors [Wilson and Yu (1979), Chung, Chang, and Chien (2001), Liu and Kardomateas (2006), among others]. Prasad (1998) employed different techniques to determine the crack path, and found that different criteria used for selecting the stress intensity factors could result in various crack paths.

Essentially, there exist two different approaches for modeling the material failure evolution, namely continuum and discrete methods. The work related to the continuum approach is based on the assumption that a continuum constitutive relation is still valid in the failure zone [Bazant and Oh (1983), Dahlbom, and Ottosen (1990), De Borst (1987), Wei and Batra (2003)]. As indicated by Schreyer, Sulsky, and Zhou (2002), the theoretical difficulty with such a method is the possible loss of ellipticity and material stability within the failure zone. The alternative approach, discrete approach, is to look upon the material failure as a displacement discontinuity with tractions being related to the displacement jumps

¹ Department of Civil and Environmental Engineering, University of Missouri-Columbia, Columbia, MO 65211-2200

² Department of Mechanical and Aerospace Engineering, University of Missouri-Columbia, Columbia, MO 65211-2200

[Feenstra, De Borst, and Rots (1991a), Feenstra, De Borst, and Rots (1991b), Corigliano (1993), Miehe and Schröder (1994), Schreyer, Sulsky, and Zhou (2002), among others]. The major disadvantage of the discrete model originates from the numerical difficulty of handling discontinuities. With the use of mesh-based methods such as the FEM and BEM, the employment of the discrete model requires a continuous change of the mesh topology as the failure evolves. However, the meshless methods are uniquely appropriate for the problems involving large deformations and the propagation of discontinuity [Belytschko, Kron-gauz, Organ, Fleming, and Krysl (1996), Atluri (2004), Atluri, Han, and Rajendran (2004), Han, Rajendran, and Atluri (2005), Gao, Liu, and Liu (2006), Ching and Chen (2006), Han, Liu, Rajendran, and Atluri (2006), Atluri, Liu, and Han (2006), Liu, Han, Rajendran, and Atluri (2006), Guo and Nairn (2006), Hagihara, Tsunori, Ikeda, and Miyazaki (2007), Sladek, Sladek, Zhang, Solec and Starek (2007) and Le, Mai-Duy, Tran-Cong, and Baker (2008)]. Without using the rigid mesh connectivity, the meshless methods do not require frequent remeshing with the failure evolution. As one of the innovative spatial discretization methods, the Material Point Method (MPM) is an extension to solid mechanics problems of a hydrodynamics code called FLIP. The motivation to develop the MPM was to simulate those challenging problems such as impact/contact, penetration and perforation with history-dependent internal state variables, as shown in the early publications about the MPM [Sulsky, Chen, and Schreyer (1994), Sulsky, Zhou, and Schreyer (1994)]. The essential idea is to take advantage of both the Eulerian and Lagrangian methods while avoiding the shortcomings of each. In comparison with the other meshless methods, the MPM appears to be less complex with a cost factor of at most twice that associated with the use of corresponding finite elements [Chen, Hu, Shen, Xin, and Brannon (2002)]. Thus, much research has recently been conducted to simulate the material failure with the use of a discrete constitutive model implemented in the MPM [Schreyer, Sulsky, and Zhou (2002), Sulsky and Schreyer (2004), Chen, Shen, Mai, and Shen (2005), among others].

Actually, according to the jumps in the kinematical field variables, the failure states can be defined as follows

$$\text{Diffusive failure: } \mathbf{v}_1 = \mathbf{v}_2, \quad \dot{\boldsymbol{\epsilon}}_1 = \dot{\boldsymbol{\epsilon}}_2 \quad (1)$$

$$\text{Localized failure: } \mathbf{v}_1 = \mathbf{v}_2, \quad \dot{\boldsymbol{\epsilon}}_1 \neq \dot{\boldsymbol{\epsilon}}_2 \quad (2)$$

$$\text{Discrete failure: } \mathbf{v}_1 \neq \mathbf{v}_2, \quad \dot{\boldsymbol{\epsilon}}_1 \neq \dot{\boldsymbol{\epsilon}}_2 \quad (3)$$

where $(\mathbf{v}_1, \mathbf{v}_2)$ and $(\dot{\boldsymbol{\epsilon}}_1, \dot{\boldsymbol{\epsilon}}_2)$ are the velocities and total strain rates on both sides of a moving surface of discontinuity. It has been shown, based on the jump forms of conservation laws, that the transition from continuous failure modes (smeared microcracking) to discontinuous failure modes (discrete macrocracking) is characterized by the evolution of localization, and identified by discontinuous bifurcation analysis [Chen (1996), Chen, Qian, and Xin (1999), Chen and Fang (2001), among others]. The evolution of localized failure could be described by a parabolic (diffusion) equation without invoking nonlocal models. A coupled wave and diffusion equation has been proposed to predict the failure wave in glass plates under impact without considering the thermo-mechanical effect, which is consistent with the experimental observations [Kanel, Bogatch, Razorenov, and Chen (2002), Chen, Feng, Xin, and Shen (2003)].

Due to the complexity involved, however, there still exists a lack of understanding on the thermo-mechanical failure process with the transition from continuous to discontinuous failure modes. Based on the previous research results as summarized above, hence, it is proposed in this paper that a bifurcation-based simulation procedure be developed to predict the failure evolution in structures subject to localized high energy loading. A decohesion model is coupled with the discontinuous bifurcation analysis based on a thermoviscoplasticity constitutive relation with thermal softening, and is implemented into the MPM code. The remaining sections of this paper are organized as follows. Section 2 describes the formulation of the proposed decohesion model, and the discontinuous bifurcation analysis for identifying the onset and orientation of thermo-mechanical discrete failure. In Section 3, the thermo-mechanical governing differential equa-

tions are briefly formulated within the framework of the MPM. In Section 4, the proposed model-based simulation procedure is verified, and the potential of the proposed procedure is demonstrated through the simulation of the failure evolution in a prestressed plate due to laser heating. Concluding remarks are given in the final section.

2 Coupled Thermo-Mechanical Modeling and Bifurcation Analysis

As demonstrated by Chen, Shen, Mai, and Shen (2005) for mechanical failure problems, a bifurcation-based decohesion model could be formulated within the framework of the MPM to simulate the transition from localization to decohesion during the failure evolution. A bifurcation-based thermomechanical decohesion model is therefore developed here, starting from the associated thermoviscoplasticity. Based on the work by Johnson and Cook (1983), the proposed thermoviscoplastic model with strain hardening and softening, strain-rate hardening and thermal softening consists of the following equations:

$$d\boldsymbol{\sigma} = \mathbf{E}(T) : (d\boldsymbol{\varepsilon} - d\boldsymbol{\varepsilon}^p) \quad (4)$$

$$f(J_2, I, \dot{\varepsilon}^p, T) = \begin{cases} 3J_2 - \left[(\sigma_y + E_h I) \left(1 + C \ln \left(\frac{\dot{\varepsilon}^p}{\dot{\varepsilon}_0} \right) \right) (1 - T_*^m) \right]^2 \\ = 0, & 0 \leq I \leq I_p; \\ 3J_2 - \left[(\sigma_p - E_s (I - I_p)) \left(1 + C \ln \left(\frac{\dot{\varepsilon}^p}{\dot{\varepsilon}_0} \right) \right) (1 - T_*^m) \right]^2 \\ = 0 & I > I_p. \end{cases} \quad (5)$$

$$d\boldsymbol{\varepsilon}^p = d\lambda \frac{\partial f}{\partial \boldsymbol{\sigma}} \quad (6)$$

$$dI = \sqrt{d\boldsymbol{\varepsilon}^p : d\boldsymbol{\varepsilon}^p} = d\lambda \quad (7)$$

where $\boldsymbol{\sigma}$ is the stress tensor, $\boldsymbol{\varepsilon}$ is the total mechanical strain tensor, $\dot{\varepsilon}_0$ is the reference strain rate, C and m are material parameters, $T_* = \frac{T - T_r}{T_m - T_r}$ normalizes the temperature T with T_m and T_r being the melting temperature of the material and room temperature, respectively, $\boldsymbol{\varepsilon}^p$ is the inelastic

strain tensor, $\mathbf{E}(T)$ is the temperature-dependent isotropic elasticity tensor, $f(J_2, I, \dot{\varepsilon}^p, T) = 0$ is the flow surface with J_2 being the second invariant of deviatoric stress tensor, I is the internal state variable, $\dot{\varepsilon}^p$ is the equivalent inelastic strain rate, σ_y and σ_p are respectively the yield strength and peak strength of the material at room temperature, I_p is the value of the internal state variable corresponding to the peak strength, E_h is the hardening modulus, E_s is the softening modulus, and λ denotes a parameter characterizing the loading process. With the use of the inelastic consistency condition, it follows from Eqs. 4-7 that

$$d\lambda = \frac{\mathbf{N} : \mathbf{E}(T) : d\boldsymbol{\varepsilon} + \frac{\partial f}{\partial \dot{\varepsilon}^p} d\dot{\varepsilon}^p + \frac{\partial f}{\partial T} dT}{\mathbf{N} : \mathbf{E}(T) : \mathbf{N} - \frac{1}{N} \frac{\partial f}{\partial T}} \quad (8)$$

$$\mathbf{N} = \frac{1}{N} \frac{\partial f}{\partial \boldsymbol{\sigma}}, \quad N = \sqrt{\frac{\partial f}{\partial \boldsymbol{\sigma}} : \frac{\partial f}{\partial \boldsymbol{\sigma}}}$$

To obtain the continuum tangent stiffness tensor for bifurcation analysis, a parameter c_f is introduced such that $d\lambda$ can be rewritten as

$$d\lambda = c_f \cdot \frac{\mathbf{N} : \mathbf{E}(T) : d\boldsymbol{\varepsilon}}{\mathbf{N} : \mathbf{E}(T) : \mathbf{N} - \frac{1}{N} \frac{\partial f}{\partial T}} \quad (9)$$

$$c_f = \frac{\mathbf{N} : \mathbf{E}(T) : d\boldsymbol{\varepsilon} + \frac{\partial f}{\partial \dot{\varepsilon}^p} d\dot{\varepsilon}^p + \frac{\partial f}{\partial T} dT}{\mathbf{N} : \mathbf{E}(T) : d\boldsymbol{\varepsilon}}$$

As a result, the tangent stiffness tensor can be found to be

$$\mathbf{E}_T(\dot{\varepsilon}^p, T, I) = \mathbf{E}(T) - H \boldsymbol{\sigma}^d \otimes \boldsymbol{\sigma}^d \quad (10)$$

where $H = c_f \cdot \frac{4G^2}{2J_2(2G - \frac{1}{N} \frac{\partial f}{\partial T})}$ with G being the shear modulus, and $\boldsymbol{\sigma}^d$ is the deviatoric stress tensor. It is assumed that the Poisson's ratio of the material, ν , is temperature-independent so that the shear modulus G is equal to $E(T)/[2(1 + \nu)]$. Based on the work of Ottosen and Runesson (1991), the localized failure condition takes the form of

$$1 - H \mathbf{a} \cdot \left(\mathbf{Q}^{el} \right)^{-1} \cdot \mathbf{a} = 0 \quad (11)$$

in which $\mathbf{a} = \mathbf{n} \cdot \boldsymbol{\sigma}^d = \boldsymbol{\sigma}^d \cdot \mathbf{n}$, and $\mathbf{Q}^{el} = \mathbf{n} \cdot \mathbf{E}(T) \cdot \mathbf{n}$ is the acoustic tensor of elasticity with \mathbf{n} being the

vector normal to the moving surface of discontinuity. In the stress space, Eq. 11 can be expressed as an ellipse, namely,

$$\frac{(\sigma - \sigma_0)^2}{A} + \frac{\tau^2}{B} = 1 \quad (12)$$

where $A = \frac{4G+3K}{3H}$ with $K = \frac{E(T)}{3(1-2\nu)}$, $B = \frac{G}{H}$, σ and τ are the normal and tangential components of the traction on the discontinuity surface, and σ_0 is the mean normal part of the stress tensor, i.e., $\sigma_0 = \sigma_{mm}/3$. On the other hand, the principal stresses and stress transformations at a given position can be illustrated by a Mohr circle, i.e.,

$$(\sigma - \sigma_c)^2 + \tau^2 = r^2 \quad (13)$$

where $\sigma_c = (\sigma_1 + \sigma_3)/2$, $r = (\sigma_1 - \sigma_3)/2$, and the principal stresses follow the order of $\sigma_1 > \sigma_2 > \sigma_3$. Geometrically, the localized failure occurs when the Mohr circle osculates the localization ellipse [Iordache and William (1998)]. By solving Eq. 12 and Eq. 13 simultaneously, hence, the critical value H^{cr} for the occurrence of the discontinuous bifurcation is determined by

$$H^{cr} = \frac{G^2 + 3KG}{3G(\sigma_0 - \sigma_c)^2 + (G + 3K)r^2} \quad (14)$$

with the corresponding critical angle of the discontinuous moving surface given by

$$\tan^2 \theta^{cr} = \frac{3G(\sigma_c - \sigma_0) - (G + 3K)r}{3G(\sigma_0 - \sigma_c) - (G + 3K)r} \quad (15)$$

It should be noted that the above solution is only valid in the case of $\frac{3G(\sigma_c - \sigma_0) - (G + 3K)r}{3G(\sigma_0 - \sigma_c) - (G + 3K)r} > 0$, as illustrated in Fig. 1(a). Otherwise, the critical state and angle should respectively be determined by

$$H^{cr} = \frac{4G + 3K}{3(\sigma_c + r - \sigma_0)^2} \quad (16)$$

and

$$\theta^{cr} = 0 \quad (17)$$

as shown in Fig. 1(b). In other words, the discontinuous bifurcation coincides with the maximum tensile stress criterion. In the MPM codes developed for the proposed model and bifurcation analysis, both Eq. 14 and Eq. 16 are checked at each

time step and at each material point. If H exceeds one of the critical values, discontinuous failure is initiated with a failure surface defined by the corresponding angle θ^{cr} which remains fixed during the evolution of failure.

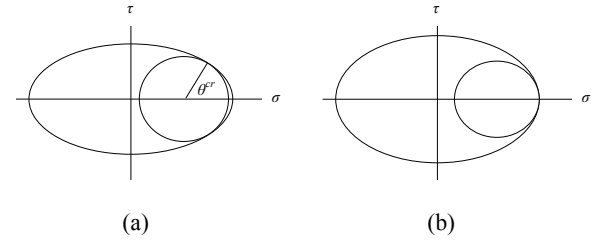


Figure 1: Geometry of the localized failure condition

Once the onset and orientation of discontinuous failure are identified via the bifurcation analysis, a decohesion constitutive model is invoked to predict the discrete failure evolution. Based on the previous work [Schreyer, Sulsky, and Zhou (2002), Chen, Shen, Mai, and Shen (2005)], the decohesion model for the thermo-mechanical problems are formulated as follows:

$$\dot{\boldsymbol{\sigma}} = \mathbf{E}(T) : (\dot{\boldsymbol{\epsilon}} - \dot{\boldsymbol{\epsilon}}^d) \quad (18a)$$

$$\dot{\boldsymbol{\tau}} = \dot{\boldsymbol{\sigma}} \cdot \mathbf{n} \quad (18b)$$

$$\dot{\mathbf{u}}^d = \lambda^d \cdot \mathbf{m} \quad (18c)$$

$$\dot{\boldsymbol{\epsilon}}^d = \frac{1}{2L_e} (\mathbf{n} \otimes \dot{\mathbf{u}}^d + \dot{\mathbf{u}}^d \otimes \mathbf{n}) \quad (18d)$$

$$F^d = \tau^e - U_0 \left[1 - (\lambda^d)^q \right] = 0 \quad (18e)$$

where $\boldsymbol{\epsilon}^d$ is the decohesion strain with the assumption that no plastic strain would occur when decohesion evolves, λ^d is a dimensionless monotonically increasing variable parameterizing the development of the decohesion, $\boldsymbol{\tau}$ is the stress vector on the decohesion surface, \mathbf{n} is the normal to the decohesion surface, the effective length L_e is the ratio of the element volume to the decohesion surface area within the element, \mathbf{u}^d is the decohesion vector used to determine the decohesion strain, and U_0 is the initial energy equal to the product of the reference decohesion \bar{u}_0 and the

reference traction $\bar{\tau}_0$. For the purpose of simplicity, the evolution function of decohesion is chosen to be associated, namely

$$\mathbf{m} = \frac{\partial F^d}{\partial \boldsymbol{\tau}} = \bar{u}_0 \frac{\mathbf{A}_d \cdot \boldsymbol{\tau}}{(\boldsymbol{\tau} \cdot \mathbf{A}_d \cdot \boldsymbol{\tau})^{1/2}} \quad (19)$$

Hence, the effective traction τ^e can be expressed as

$$\tau^e = \boldsymbol{\tau} \cdot \mathbf{m} = \bar{u}_0 (\boldsymbol{\tau} \cdot \mathbf{A}_d \cdot \boldsymbol{\tau})^{1/2} \quad (20)$$

The positive definite tensor of material parameters, \mathbf{A}_d , in the two-dimensional local normal-tangential coordinate system with respect to the failure surface, takes the form of

$$[\mathbf{A}_d] = \bar{\tau}_0^2 \begin{bmatrix} 1/\tau_{nf}^2 & 0 \\ 0 & 1/\tau_{tf}^2 \end{bmatrix} \quad (21)$$

with τ_{nf} and τ_{tf} denoting the failure initiation values for pure tension and shear cases, respectively. At the initiation of decohesion, the consistency condition, i.e. Eq. 18e, yields $\tau^e = U_0 = \bar{u}_0 \bar{\tau}_0$. As a result, it follows that

$$\frac{\tau_n^2}{\tau_{nf}^2} + \frac{\tau_t^2}{\tau_{tf}^2} = 1 \quad (22)$$

where τ_n and τ_t are the normal and tangential traction components on the failure surface at the initiation of decohesion, and they can be determined via the bifurcation analysis. With the assumption of $c_m = \frac{\tau_{tf}}{\tau_{nf}}$, τ_{nf} and τ_{tf} can be found for a given value of c_m since τ_n and τ_t are already known through the bifurcation analysis. From the definition of c_m , it can be noticed that different values of c_m result in various failure modes. For example, $c_m = 10$ can be used for mode I failure, 0.1 for mode II failure, and 1.0 for mix mode failure. To meet the consistency condition of $F^d = 0$, a one-step algorithm is designed by taking a Taylor expansion of F^d about the trial state to the order $(\Delta\lambda^d)^2$, namely

$$F^d = \frac{\partial F^d}{\partial \lambda} \Big|_{tr} \Delta\lambda^d + \left\{ \tau^e - U_0 \left[1 - (\lambda^d)^q \right] \right\} \Big|_{tr} + \text{O} \left((\Delta\lambda^d)^2 \right) = 0 \quad (23)$$

Given the total mechanical strain increment at each time step and at each material point, it is assumed that no decohesion occurs in the beginning of the time step in order to get the trial stresses and traction through Eq. 18a and Eq. 18b, and the value of F^d can then be determined based on the trial state and existing value of λ^d . If $F^d \leq tol$ with tol being a small positive number, the step is elastic without further decohesion. Otherwise, $\Delta\lambda^d$ is obtained from Eq. 23, and decohesion variables are updated in the end of the time step.

In summary, an associated thermoviscoplasticity model combined with decohesion has been formulated, and the discontinuous bifurcation analysis could be performed to identify the onset and orientation of the discrete failure. To accommodate the continuous and discontinuous failure modes in a unified framework, the proposed constitutive models are implemented into the MPM, as discussed in the next section.

3 The MPM for Simulating Thermo-Mechanical Failure Evolution

For numerical simulations of multi-physics involved in thermo-mechanical failure evolution, a robust spatial discretization procedure with flexible mesh connectivity is a necessity. In the MPM, the equations of motion are solved on a computational grid which could be used to discretize the heat conduction equation. Therefore, the employment of the MPM allows simulating wave propagation and heating conduction in a single computational domain. In other words, the coupled thermo-mechanical constitutive model discussed in the last section could be implemented within the framework of the MPM. To make this point clear, the essential steps of the proposed simulation procedure for the thermo-mechanical problems are described below.

The thermo-mechanical governing differential equations for a solid body without internal energy source consist of conservation equations for mass, momentum and energy, namely

$$\frac{d\rho}{dt} + \rho \nabla \cdot \mathbf{v} = 0 \quad (24)$$

$$\rho \mathbf{a} = \nabla \cdot \boldsymbol{\sigma} + \rho \mathbf{b} \quad (25)$$

and

$$\nabla^2 T = \frac{1}{\hat{\alpha}} \frac{\partial T}{\partial t} \quad (26)$$

together with constitutive equations. In the above equations, ρ is the mass density, $\mathbf{a}(\mathbf{x}, t)$ the acceleration, $\mathbf{v}(\mathbf{x}, t)$ the velocity, $\mathbf{b}(\mathbf{x}, t)$ the body force, $\boldsymbol{\sigma}(\mathbf{x}, t)$ the stress tensor, $T(\mathbf{x}, t)$ the temperature, and $\hat{\alpha}(T)$ the temperature-dependent thermal diffusivity of the material. The vector \mathbf{x} is the current position at time t of the material point which is initially located at the position \mathbf{X} . These governing equations can be solved for given initial conditions and appropriate conditions on the boundary $\partial\Omega$. The mechanical boundary conditions take the form of

$$\mathbf{u}(\mathbf{x}, t) = \mathbf{g}(t), \quad \text{on } \partial\Omega_u \quad (27)$$

$$\boldsymbol{\sigma}(\mathbf{x}, t) \cdot \mathbf{n}_b = \boldsymbol{\tau}_b(t), \quad \text{on } \partial\Omega_\tau \quad (28)$$

where \mathbf{n}_b denotes the unit outward normal to the boundary, the displacement $\mathbf{g}(t)$ and traction $\boldsymbol{\tau}_b(t)$ are prescribed on $\partial\Omega_u$ and $\partial\Omega_\tau$, respectively. Generally, the thermal boundary conditions include prescribed surface temperature and heat flux, and the heat convection and radiation on the boundary. With the small deformation assumption and the consideration of the thermal expansion, the mechanical strain rate tensor is defined to be

$$\frac{d\boldsymbol{\epsilon}}{dt} = \frac{1}{2} \left[\nabla \mathbf{v} + (\nabla \mathbf{v})^T \right] - \alpha(T) \frac{dT}{dt} \mathbf{I} \quad (29)$$

where \mathbf{I} is a unity tensor, and $\alpha(T)$ is the temperature-dependent thermal expansion coefficient of the material. The strain rate in Eq. 29 can then be employed to update the stress at a material point with the use of an appropriate constitutive model. A solid body is divided into a finite set of mass points, each of which contains a fixed amount of mass at all times. For a finite collection of N_p material points with a fixed mass M_p at each point, it follows that

$$\rho(\mathbf{x}, t) = \sum_{p=1}^{N_p} M_p \delta(\mathbf{x} - \mathbf{X}_p(t)) \quad (30)$$

where δ is the Dirac delta function, and $\mathbf{X}_p(t)$ is the position of material point p at time t . Since

M_p is fixed, the mass conservation equation is automatically satisfied. Through multiplying Eq. 25 by a test function \mathbf{w} and integrating over the current configuration Ω , we obtain

$$\int_{\Omega} \rho \mathbf{w} \cdot \mathbf{a} d\Omega = - \int_{\Omega} \rho \boldsymbol{\sigma}^s : \nabla \mathbf{w} d\Omega + \int_{\partial\Omega_\tau} \boldsymbol{\tau}_b \cdot \mathbf{w} dS + \int_{\Omega} \rho \mathbf{w} \cdot \mathbf{b} d\Omega \quad (31)$$

with $\rho \boldsymbol{\sigma}^s = \boldsymbol{\sigma}$. The use of Eq. 30 and Eq. 31 yields

$$\begin{aligned} & \sum_{p=1}^{N_p} M_p \mathbf{w}(\mathbf{X}_p(t), t) \cdot \mathbf{a}(\mathbf{X}_p(t), t) = \\ & - \sum_{p=1}^{N_p} M_p \boldsymbol{\sigma}^s(\mathbf{X}_p(t), t) : \nabla \mathbf{w}(\mathbf{x}, t) \Big|_{\mathbf{x}=\mathbf{X}_p(t)} \\ & + \int_{\partial\Omega_\tau} \mathbf{w} \cdot \boldsymbol{\tau}_b dS \\ & + \sum_{p=1}^{N_p} M_p \mathbf{w}(\mathbf{X}_p(t), t) \cdot \mathbf{b}(\mathbf{X}_p(t), t) \quad (32) \end{aligned}$$

In the MPM, a background computational mesh is defined to calculate the gradient terms, as shown in Fig. 2(a). For two-dimensional problems, the background mesh comprises a set of 4-node cells as illustrated in Fig. 2(b). The use of conventional 4-node finite element shape functions $N_i(\mathbf{x})$, $i=1, 2, 3$ and 4, results in the following interpolations of the field variables and test function:

$$\mathbf{x} = \sum_{i=1}^4 \mathbf{x}_i(t) N_i(\mathbf{x}) \quad (33a)$$

$$\mathbf{u}(\mathbf{x}, t) = \sum_{i=1}^4 \mathbf{u}_i(t) N_i(\mathbf{x}) \quad (33b)$$

$$\mathbf{v}(\mathbf{x}, t) = \sum_{i=1}^4 \mathbf{v}_i(t) N_i(\mathbf{x}) \quad (33c)$$

$$\mathbf{a}(\mathbf{x}, t) = \sum_{i=1}^4 \mathbf{a}_i(t) N_i(\mathbf{x}) \quad (33d)$$

$$\mathbf{w}(\mathbf{x}, t) = \sum_{i=1}^4 \mathbf{w}_i(t) N_i(\mathbf{x}) \quad (33e)$$

where $\mathbf{x}_i(t)$, $\mathbf{u}_i(t)$, $\mathbf{v}_i(t)$ and $\mathbf{a}_i(t)$ are the nodal coordinates, displacements, velocities and accelerations at time t , respectively, and $\mathbf{w}_i(t)$ is the test function at grid nodes. As a result, Eq. 32 at time t^k ($k=1, 2, 3, \dots$) becomes

$$\begin{aligned} & \sum_{i=1}^4 \mathbf{w}_i^k \cdot \sum_{j=1}^4 m_{ij}^k \mathbf{a}_j^k = \\ & - \sum_{i=1}^4 \mathbf{w}_i^k \cdot \sum_{p=1}^{N_p} M_p \boldsymbol{\sigma}_p^{s,k} \cdot \nabla N_i(\mathbf{x})|_{\mathbf{x}=\mathbf{X}_p^k} \\ & + \sum_{i=1}^4 \mathbf{w}_i^k \cdot \boldsymbol{\tau}_i^k + \sum_{i=1}^4 \mathbf{w}_i^k \cdot \mathbf{b}_i^k \end{aligned} \quad (34)$$

where a superscript k denotes the evaluation at time t^k , and also

$$m_{ij}^k = \sum_{p=1}^{N_p} M_p N_i(\mathbf{X}_p^k) N_j(\mathbf{X}_p^k) \quad (35)$$

$$\hat{\boldsymbol{\tau}}_i^k = \int_{\partial\Omega_\tau} N_i(\mathbf{x}) \boldsymbol{\tau}_b(\mathbf{x}, t^k) dS \quad (36)$$

$$\boldsymbol{\sigma}_p^{s,k} = \boldsymbol{\sigma}^s(\mathbf{X}_p, t^k) \quad (37)$$

$$\mathbf{b}_i^k = \sum_{p=1}^{N_p} M_p \mathbf{b}(\mathbf{X}_p, t) N_i(\mathbf{X}_p^k) \quad (38)$$

Because the components of \mathbf{w}_i^k are arbitrary except those corresponding to the essential boundary conditions, the weak form of the governing differential equations then reduces to

$$\sum_{j=1}^4 m_{ij}^k \mathbf{a}_j^k = \mathbf{f}_i^{int,k} + \mathbf{f}_i^{ext,k} \quad (39)$$

with

$$\mathbf{f}_i^{int,k} = - \sum_{p=1}^{N_p} M_p \mathbf{G}_{ip}^k \cdot \boldsymbol{\sigma}_p^{s,k} \quad (40)$$

$$\mathbf{f}_i^{ext,k} = \mathbf{b}_i^k + \hat{\boldsymbol{\tau}}_i^k \quad (41)$$

$$\mathbf{G}_{ip}^k = \nabla N_i(\mathbf{x})|_{\mathbf{x}=\mathbf{X}_p^k} \quad (42)$$

For simplicity, the consistent mass matrix m_{ij}^k is replaced with the lumped mass matrix m_i^k , namely,

$$m_i^k = \sum_{p=1}^{N_p} M_p N_i(\mathbf{X}_p^k) \quad (43)$$

Then, Eq. 39 becomes

$$m_i^k \mathbf{a}_i^k = \mathbf{f}_i^{int,k} + \mathbf{f}_i^{ext,k} \quad (44)$$

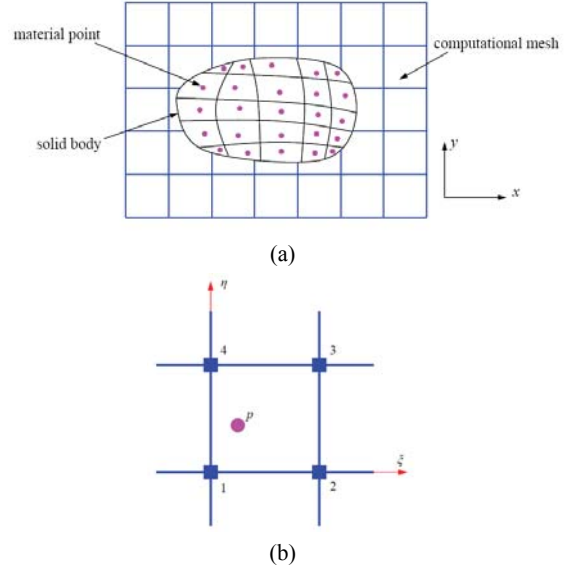


Figure 2: The MPM discretization and computational mesh in two dimensions: (a) a solid body represented by material points and a defined computational mesh, (b) one 4-node cell and the logical coordinate system

An explicit time integrator is used to solve Eq. 44 to obtain the nodal accelerations. To ensure stability, a time step should not be larger than the critical time step, i.e., the value of the smallest cell size divided by the wave speed of the material. After Eq. 44 is solved on the cell nodes, the material point position is updated by mapping the grid node velocity to the material point with the use of the nodal shape functions. The total strain increment of the material point is then computed from the grid node velocities, and the gradient of the shape functions evaluated at the updated material point position. On the other hand, the constructed computational mesh is also used to solve the heat conduction equation, Eq. 26, with the standard finite difference method. The temperature at each material point might be computed from the nodal temperature and nodal shape functions or simply chosen to be the average of temperature at nodes

of the cell containing that point. Once the increment of strain tensor is determined, the corresponding stress increment could be found through the thermomechanical constitutive model as described in the last section. The computation cycle in the current time step is complete after the material points are updated. The computational background mesh used in the current time step might be replaced with a newly defined one, if desired, for the next computation cycle.

4 Verification and Demonstration

To verify the proposed model-based simulation procedure, a transient thermoelastic problem for a semi-infinite medium, for which the analytical solutions are available, is considered. As illustrated in Fig. 3, an elastic medium occupying a half-space ($x > 0$) is suddenly exposed to a temperature of $T_0 = 100^\circ\text{C}$ on the surface $x=0$ at time $t=0^+$ and the surface temperature remains constant thereafter. The problem is solved within the context of classic uncoupled thermoelasticity by using the finite difference method for thermal diffusion and the MPM for wave propagation. Because the half-body is constrained to the uniaxial displacement only, the problem is essentially one-dimensional, and the body can be modeled by a bar. In this case, Young's modulus E and Poisson's ratio ν of the material are set to be $100 \text{ N}\cdot\text{m}^{-2}$ and 0.25 , respectively. In addition, it is assumed that mass density $\rho = 1 \text{ kg}\cdot\text{m}^{-3}$, specific heat capacity $c = 1 \text{ J}\cdot\text{kg}^{-1}\cdot\text{K}^{-1}$ and thermal conductivity $k = 1 \text{ W}\cdot\text{m}^{-1}\cdot\text{K}^{-1}$. The total length of the bar is chosen so that no temperature change will occur at the right end of the bar during the time period of interest. The computational mesh for both the finite difference and MPM consists of square cells with a side length of $4.5 \times 10^{-3} \text{ m}$. The bar is discretized with one material point per cell. The time steps for the finite difference and MPM are set to be $2.0 \times 10^{-6} \text{ s}$ and $1.0 \times 10^{-4} \text{ s}$, respectively, based on the consideration of the numerical stability and accuracy. The computation is carried out with a plane strain assumption. For convenience, the solutions are presented in terms of dimensionless variables defined by Sternberg and Chakravorty (1959). Fig. 4 gives the time history of temper-

ature at dimensionless coordinate $\xi = 1.0$. Fig. 5 displays the time history of the axial stress and displacement at $\xi = 1.0$. It can be observed that there is a good agreement between the numerical solutions obtained by the proposed thermo-mechanical simulation method and the analytical solutions. As can be seen from this example, the thermoelasticity problem involving the heat conduction and wave propagation can be solved in a single computational domain. Different constitutive models can be invoked to update the stresses at material points for given strains. Since there is no fixed connectivity between the material points and background mesh, it appears to be reasonable to simulate the thermo-mechanical failure evolution with the proposed model-based simulation procedure, as demonstrated next.

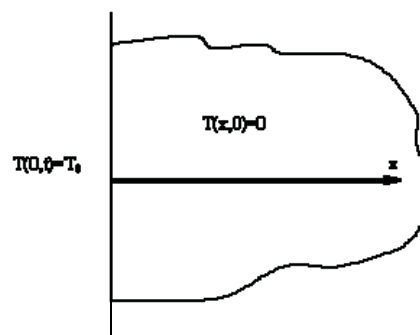


Figure 3: An elastic half-space medium subject to surface heating

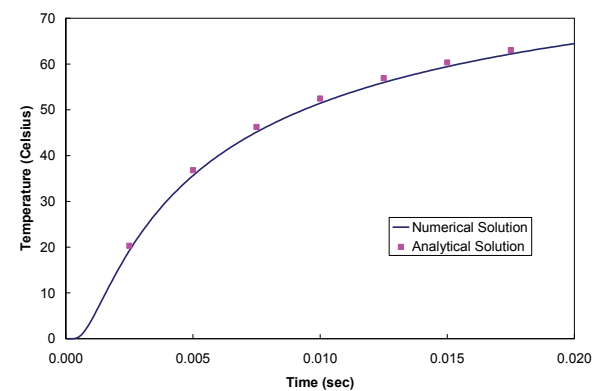


Figure 4: Time history of temperature at dimensionless coordinate $\xi = 1.0$

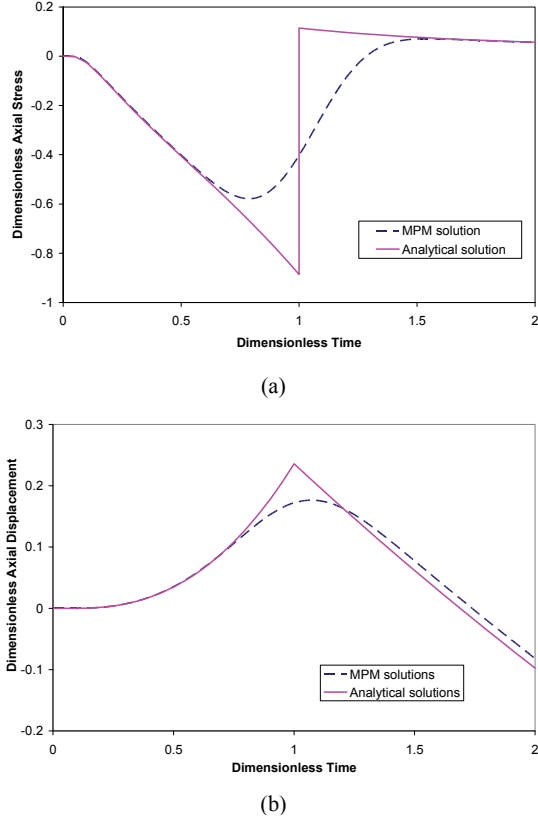


Figure 5: Time history of the axial stress and displacement at dimensionless coordinate $\xi=1.0$: (a) axial stress time history, (b) axial displacement time history

Fig. 6 shows a prestressed square plate (Aluminum 2024) subject to laser heating in the center. The plate has a side length of 0.1m, and the irradiated circular area has a radius of 1.5cm. It is assumed that the temperature of the irradiated area linearly increases from room temperature 20°C to 400°C during a time period of 3×10^{-3} second, and the temperature field is independent of the z -coordinate. The computational grid consists of square cells with a side length of 0.2cm, and each cell contains one material point initially. Thus, the plate is discretized by 2500 material points. The time step is chosen as 1×10^{-8} s to meet the stability criteria for both the finite difference method and MPM.

It has been recognized that some material properties significantly vary with the temperature. Here, the Young's modulus at various tempera-

ture degrees is shown in Fig. 7. Also, the specific heat and thermal conductivity of the material are temperature-dependent, as illustrated in Fig. 8 and Fig. 9. The mean thermal expansion coefficient of Aluminum 2024 between 20°C and 427°C is chosen to be $26.1 \times 10^{-6} \text{ K}^{-1}$ for the simulation. The values of other material parameters are taken from those measured at room temperature with mass density $\rho=2780\text{kg}\cdot\text{m}^{-3}$, Poisson's ratio $\nu=0.33$, hardening modulus $E_h=1.075 \times 10^9\text{Pa}$, softening modulus $E_s=E_h/10$, yield stress $\sigma_y=294\text{MPa}$, and peak stress $\sigma_p=438\text{MPa}$. In addition, material parameters C and m in Eq. 5 are respectively 0.015 and 1.0, and the melting temperature for Aluminum 2024 is 502°C. For the discrete constitutive model, it is assumed that q , c_m and \bar{u}_0 are 1.0, 10.0 and 0.8×10^{-6} , respectively, for the purpose of demonstration.

Two pre-stressed states, uniaxial tension and biaxial tension, are considered. The initial effective

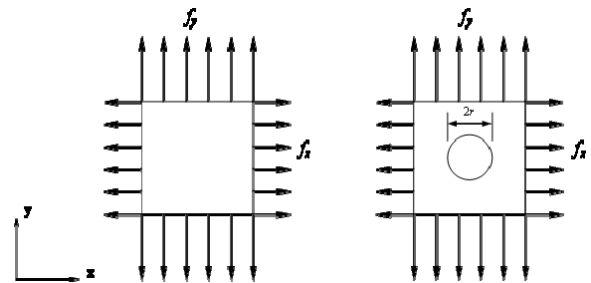


Figure 6: A prestressed plate subject to laser heating in the center

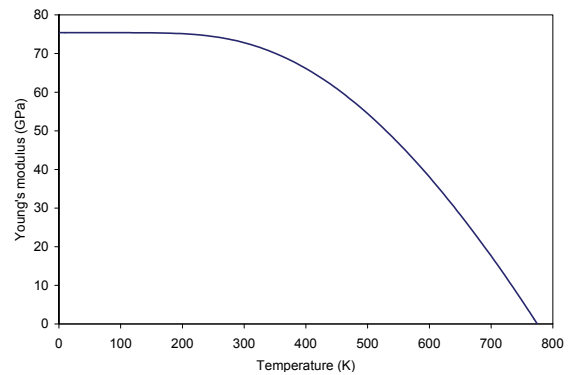


Figure 7: Young's modulus at various temperatures

stresses in these two cases are both at 80% of the yield stress of the material at the room temperature, as listed in Tab. 1. To obtain the static pre-stressed state, the external mechanical forces are first applied to the plate in a ramp-type way as shown in Fig. 10. The magnitude of the force linearly increases from zero to the desired value in a duration of 2×10^{-3} s and keeps constant thereafter. Then, the laser begins to irradiate the plate at the time of 5×10^{-3} s and lasts 3×10^{-3} s so that the total simulation time is 8×10^{-3} s. Fig. 11 gives the time-history of the stress σ_x at the center of the plate under the uniaxial tension only. It is observed that the oscillation of stress σ_x gradually decreases and the stress finally lies in the range between $0.95 f_x$ and $1.05 f_x$. Hence, it can be concluded that the employment of the ramp-type loading function is reasonable. The deformation fields for both cases at different times are illustrated in Fig. 12 and Fig. 13, where the displacements are respectively magnified by 10 times and 30 times in the x - and y -direction to clearly show the deformation pattern of the plate.

Table 1: Initial pre-stressed state

Case	f_x (MPa)	f_y (MPa)	Effective stress (MPa)
Uniaxial tension	235.2	0	235.2
Biaxial tension	271.6	135.8	235.2

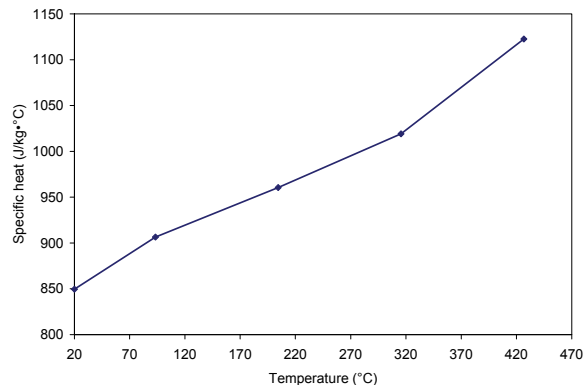


Figure 8: Specific heat at various temperatures

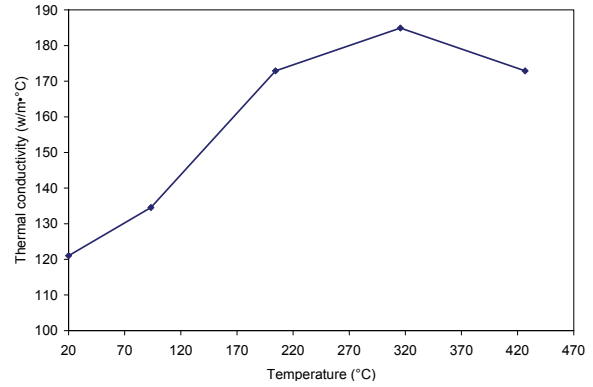


Figure 9: Thermal conductivity at various temperatures

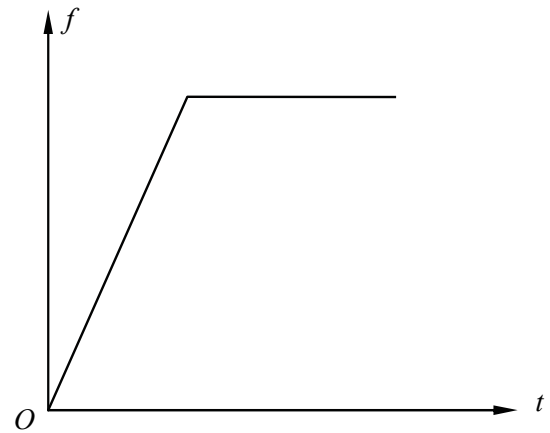


Figure 10: The ramp-type external mechanical force

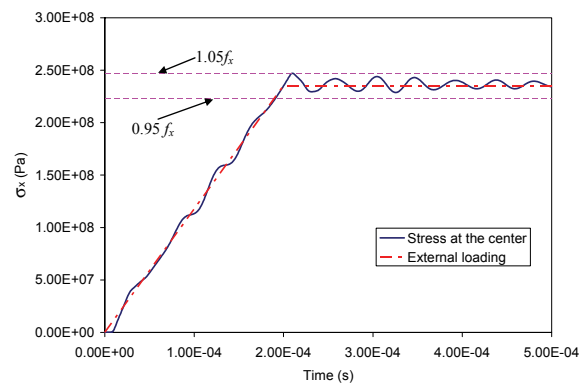
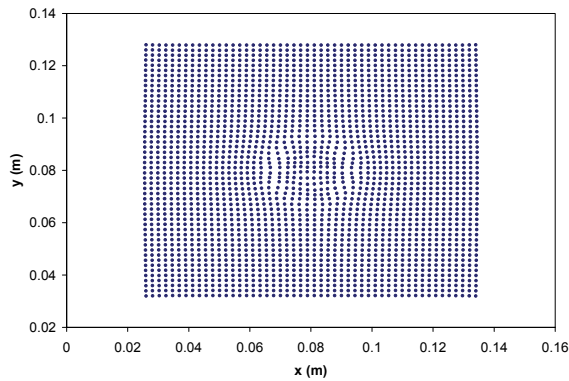


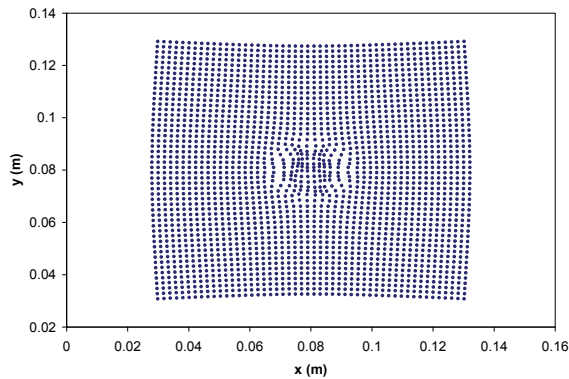
Figure 11: Time-history of stress σ_x at the center of the plate

As can be seen from Fig. 12 and Fig. 13, cracks first occur on the interface, i.e., the horizontal

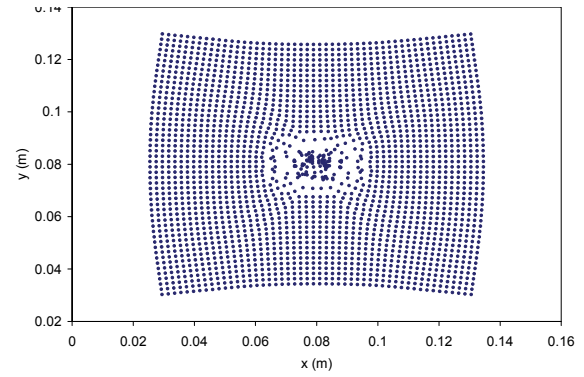
peak points of the circular irradiated area, and the cracks are perpendicular to the major mechanical loading direction. With the evolution of cracks, it can be found that decohesion only occurs within the irradiated area until all material points in that area finally fail and no further crack development could be observed. In our viewpoint, this phenomenon might be due to several factors: First, the short-time laser heating leads to the localization of the temperature field because of the inadequate heat conduction in the plate, which can be observed in Fig. 14. An interface along the circumference of the heated zone is then formed owing to the temperature-dependent material properties. Accordingly, the decohesion is initially found on the interface due to different material properties and a high stress gradient. Second, the plate (Aluminum 2024) has a low melting temperature and a relatively small absolute value of the



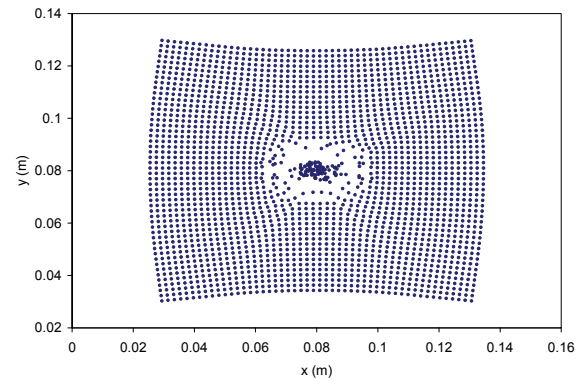
(a) 0.13×10^{-3} s after laser heating



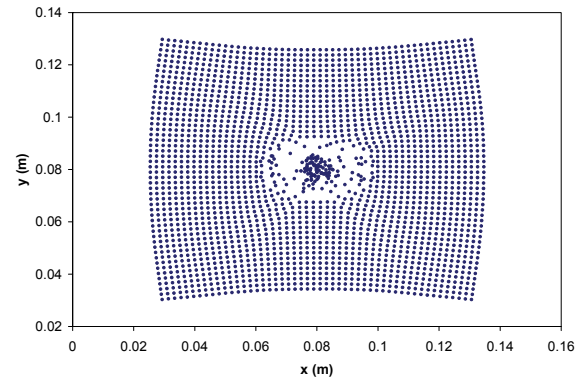
(b) 0.15×10^{-3} s after laser heating



(c) 0.2×10^{-3} s after laser heating



(d) 0.25×10^{-3} s after laser heating

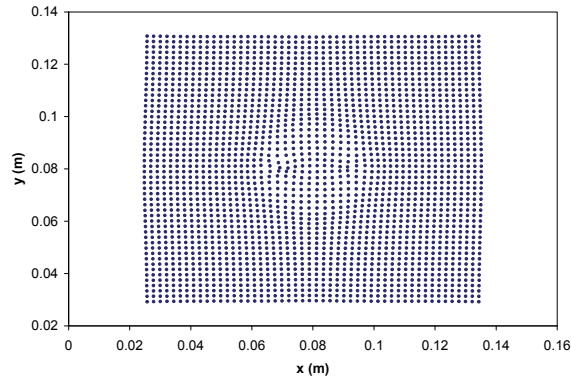


(e) 0.3×10^{-3} s after laser heating

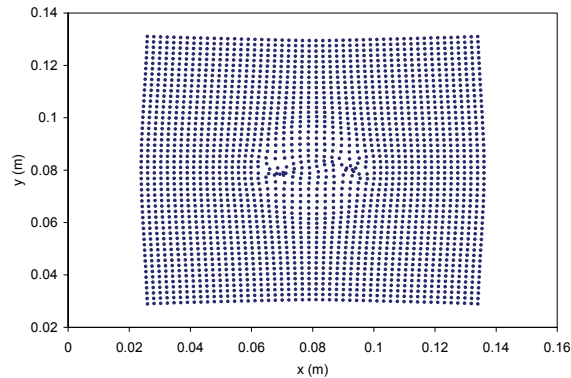
Figure 12: Deformation fields of the plate for the uniaxial tension case at different times

thermal stress per unit temperature change. The thermal stress level is not high enough to lead to the transition from continuous failure to discontinuous failure in the unheated region of the plate. Therefore, there is no any crack development observed outside the irradiated area throughout the

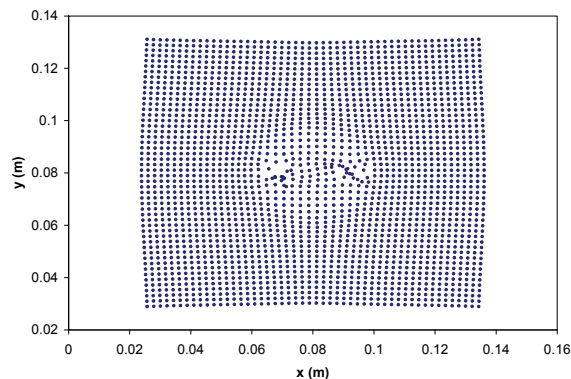
simulations. On the other hand, by comparing Fig. 12 and Fig. 13, a similar deformation pattern can be observed, except that the initial cracks occur later in the biaxial tension case and decohesion is severer in the uniaxial tension situation with the same irradiation time.



(a) 0.23×10^{-3} s after laser heating



(b) 0.25×10^{-3} s after laser heating



(c) 0.3×10^{-3} s after laser heating

Figure 13: Deformation fields for the biaxial tension case at different times

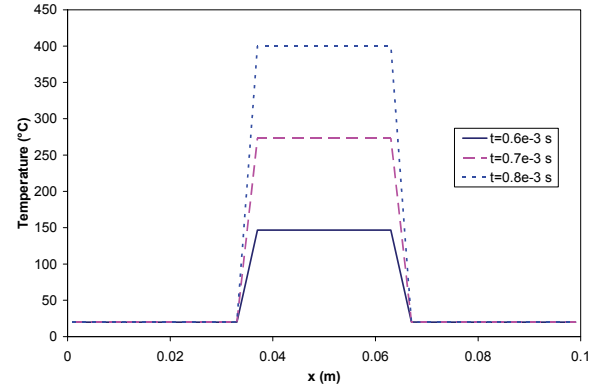


Figure 14: Temperature profile along the horizontal symmetrical axis of the plate at different times

5 Concluding Remarks

To predict the failure evolution in plate structures due to localized heating, a coupled thermo-mechanical constitutive model with decohesion has been developed in this paper. Based on a thermoviscoplastic model, which takes account of strain hardening and softening, strain-rate hardening and thermal softening, the continuum tangent stiffness tensor has been formulated so that a discontinuous bifurcation analysis could be performed to identify the onset of the transition from continuous to discontinuous failure modes as well as the orientation of the discontinuous failure mode. The thermo-mechanical governing differential equations have been discretized within the framework of the MPM so that different gradient and divergence operators could be treated in a single computational domain for given boundary and initial data. The proposed model-based simulation procedure has been verified with a transient thermoelasticity problem. To demonstrate its potential in the thermomechanical failure simulation, the proposed procedure has been used to model the failure evolution in a pre-stressed plate subject to laser irradiation. It appears from this preliminary study that thermo-mechanical decohesion depends on the initial pre-stressed state, the magnitude and duration of thermal loading, as well as the material properties. An integrated analytical, experimental and numerical effort is required to further verify and improve the proposed procedure.

Acknowledgement: This work was partially supported by the Air Force Research Laboratory.

References

Atluri, S. N. (2004): *The Meshless Method (MLPG) for Domain & BIE Discretizations*. Norcross, GA: Tech Science Press.

Atluri, S. N.; Han, Z. D.; Rajendran, A. M. (2004): A New Implementation of the Meshless Finite Volume Method, Through the MLPG “Mixed” Approach. *CMES: Computer Modeling in Engineering & Sciences*, Vol. 6, pp. 491-514.

Atluri, S.N.; Liu, H.T.; Han, Z.D. (2006): Meshless Local Petrov-Galerkin (MLPG) Mixed Finite Difference Method for Solid Mechanics. *CMES: Computer Modeling in Engineering & Sciences*, Vol. 15, pp. 1-16.

Bazant, Z. P.; Oh, B. H. (1983): Crack Band Theory for Fracture of Concrete. *Materials and Structures*, vol. 16, pp. 155–177.

Belytschko, T.; Krongauz, Y.; Organ, D.; Fleming, M.; Krysl, P. (1996): Meshless methods: An overview and recent developments. *Computer Methods in Applied Mechanics and Engineering*, vol. 139, pp: 3–48.

Beraun, J.; Chen, J. K.; Tzou, D. Y. (1999): Thermo-mechanical Fracture of Pressurized Vessels Induced by a Localized Energy Source. *Journal of Pressure Vessel Technology*, vol. 121, pp: 160-169.

Chen, Z. (1996): Continuous and Discontinuous Failure Modes. *Journal of Engineering Mechanics*, vol. 122, pp: 80-82.

Chen, Z.; Fang, H. E. (2001): A Study on the Link between Coupled Plasticity/Damage and Decohesion for Multi-Scale Modeling. *Journal of Mechanical Engineering Science - Proceedings of the Institution of Mechanical Engineers Part C*, vol. 215, pp: 259-263.

Chen, Z.; Feng, R.; Xin, X.; Shen, L. (2003): A Computational Model for Impact Failure with Shear-Induced Dilatancy. *International Journal for Numerical Methods in Engineering*. Vol. 56, pp: 1979-1997.

Chen, Z.; Hu, W.; Shen, L.; Xin, X.; Bran-

non, R. (2002): An Evaluation of the MPM for Simulating Dynamic Failure with Damage Diffusion. *Engineering Fracture Mechanics*, vol. 69, pp: 1873-1890.

Chen, Z.; Qian, D.; Xin, X. (1999): A Study of Localization Problems Based on the Transition between Governing Equations. *International Journal of Advances in Structural Engineering*, vol. 2, pp: 289-304.

Chen, Z.; Shen, L.; Mai, Y.-W.; Shen, Y.-G. (2005): A Bifurcation-based Decohesion Model for Simulating the Transition from Localization to Decohesion with the MPM. *Journal of Applied Mathematics and Physics (ZAMP)*, vol. 56, pp: 908-930.

Ching, H.K.; Chen, J.K. (2006): Thermomechanical Analysis of Functionally Graded Composites under Laser Heating by the MLPG Method *CMES: Computer Modeling in Engineering & Sciences*, Vol. 13, pp. 199-218.

Chung, Y.-L.; Chang, C.-Y.; Chien, C.-C. (2001): Boundary element analysis of interface cracks subjected to non-uniform thermal loading. *International Journal of Fracture*, vol. 110, pp: 137-154.

Corigliano, A. (1993): Formulation, identification and use of interface models in the numerical analysis of composite delamination. *International Journal of Solids and Structures*, vol. 30, pp: 2779–2811.

Dahlbom, O.; Ottosen, N. S. (1990): Smearred Crack Analysis Using Generalized Fictitious Crack Model. *Journal of Engineering Mechanics*, vol. 116, pp: 55–76.

De Borst, R. (1987): Smearred cracking, plasticity, creep, and thermal loading—A unified approach. *Computer Methods in Applied Mechanics and Engineering*, vol. 62, pp: 89–110.

Erdogan, F.; Sih, G. C. (1963): On the Crack Extension in Plates Under Plane loading and Transverse Shear. *Journal of Basic Engineering*, vol. 85, pp: 519-527.

Feenstra, P. H.; De Borst, R.; Rots, J. G. (1991a): Numerical Study of Crack Dilatancy. I: Models and Stability Analysis. *Journal of Engineering Mechanics*, vol. 117, pp: 733-753.

- Feenstra, P.H.; De Borst, R.; Rots, J. G.** (1991b): Numerical Study of Crack Dilatancy. II: Applications. *Journal of Engineering Mechanics*, vol. 117, pp: 754-769.
- Gao, L.; Liu, K.; Liu, Y.** (2006): Applications of MLPG Method in Dynamic Fracture Problems. *CMES: Computer Modeling in Engineering & Sciences*, Vol. 12, pp. 181-196.
- Guo, Y.J.; Narin, J.A.** (2006): Three-Dimensional Dynamic Fracture Analysis Using the Material Point Method. *CMES: Computer Modeling in Engineering & Sciences*, Vol. 16, pp. 141-156.
- Han, Z.D.; Liu, H.T.; Rajendran, A.M.; Atluri, S.N.** (2006): The Applications of Meshless Local Petrov-Galerkin (MLPG) Approaches in High-Speed Impact, Penetration and Perforation Problems. *CMES: Computer Modeling in Engineering & Sciences*, Vol. 14, pp. 119-128.
- Han, Z.D.; Rajendran, A.M.; Atluri, S.N.** (2005): Meshless Local Petrov-Galerkin (MLPG) Approaches for Solving Nonlinear Problems with Large Deformations and Rotations. *CMES: Computer Modeling in Engineering & Sciences*, Vol. 10, pp. 1-12.
- Hagihara, S.; Tsunori, M.; Ikeda, T.; Miyazaki, N.;** (2007): Application of Meshfree Method to Elastic-Plastic Fracture Mechanics Parameter Analysis. *CMES: Computer Modeling in Engineering & Sciences*, Vol. 17, pp. 63-72.
- Iordache, M. M.; William, K.** (1998): Localized Failure Analysis in Elastoplastic Cosserat Continua. *Computer Methods in Applied Mechanics and Engineering*, vol. 151, pp: 559-586.
- Johnson, G. R.; Cook, W. H.** (1983): A Constitutive Model and Data for Metals Subjected to Large Strains, High Strain Rates and High Temperatures. In: *Proc. 7th International Symposium on Ballistics*, Hague, Netherlands, pp. 541-547.
- Kanel, G. I.; Bogatch, A. A.; Razorenov, S. V.; Chen, Z.** (2002): Transformation of Shock Compression Pulses in Glass due to the Failure Wave Phenomena. *Journal of Applied Physics*, vol. 92, pp: 5045-5052.
- Le, P.; Mai-Duy, N.; Tran-Cong, T.; Baker, G.** (2008): A Meshless Modeling of Dynamic Strain Localization in Quasi-Brittle Materials Using Radial Basis Function Networks. *CMES: Computer Modeling in Engineering & Sciences*, Vol. 25, pp. 43-68.
- Liu, H.T.; Han, Z.D.; Rajendran, A.M.; Atluri, S.N.** (2006): Computational Modeling of Impact Response with the RG Damage Model and the Meshless Local Petrov-Galerkin (MLPG) Approaches. *CMC: Computers, Materials & Continua*, Vol. 4, pp. 43-54.
- Liu L.; Kardomateas, G. A.** (2006): A Dislocation Approach for the Thermal Stress Intensity Factors of a Crack in an Infinite Anisotropic Medium under Uniform Heat Flow. *Composites: Part A*, vol. 37, pp: 989-996.
- Miehe, C.; Schröder, J.** (1994): Post-critical discontinuous localization analysis of small strain softening elastoplastic solids. *Archive of Applied Mechanics*, vol. 64, pp: 267-285.
- Ottosen, N.; Runesson, K.** (1991): Properties of discontinuous bifurcation solutions in elastoplasticity. *Internal Journal of Solids and Structures*, vol. 27, pp: 401-421.
- Prasad, N. N. V.** (1998): *Thermomechanical Crack Growth using Boundary Elements*. Southampton, UK: Computational Mechanics Publications/WIT Press.
- Schreyer, H. L.; Sulsky, D.L.; Zhou, S. J.** (2002): Modeling Delamination as a Strong Discontinuity with the Material Point Method. *Computer Methods in Applied Mechanics and Engineering*, vol. 191, pp: 2483-2507.
- Sih, G. C.** (1973): A Special Criterion for Crack Propagation, In: Sih, G.C. (ed), *Methods of Analysis and Solutions of Crack Problems*, vol. 1, pp: 21-45.
- Sladek, J.; Sladek, V.; Zhang, Ch.; Sulek, P.; Starek, L.;** (2007): Fracture Analyses in Continuously Nonhomogeneous Piezoelectric Solids by the MLPG. *CMES: Computer Modeling in Engineering & Sciences*, Vol. 19, pp. 247-262.
- Sternberg, E.; Chakravorty, J. G.** (1959): On Inertia Effects in a Transient Thermoelastic Problem. *Journal of Applied Mechanics*, vol. 26, pp: 503-509.

Sulsky, D.; Chen, Z.; Schreyer, H.L. (1994): A Particle Method for History-dependent Materials. *Computer Methods in Applied Mechanics and Engineering*, vol. 118, pp: 179-196.

Sulsky, D.; Schreyer, H. (2004): MPM Simulation of Dynamic Material Failure with a Cohesive Constitutive Model. *European Journal of Mechanics A/Solids*, vol. 23, pp: 423-445.

Sulsky, D.; Zhou, S. J.; Schreyer, H. L. (1995): Application of Particle-in-cell Method to Solid Mechanics. *Computer Physics Communications*, vol. 87, pp: 236-252.

Wei, Z. G.; Batra, R. C. (2003): Deformation of an Axially Loaded Thermoviscoplastic Bar due to Laser Heating. *Journal of Thermal Stresses*, vol. 26, pp: 701-712.

Wilson, W. K.; Yu, I.-W. (1979): The use of the J-integral in thermal stress crack problems. *International Journal of Fracture*, vol. 15, pp: 377-387.

